Check for updates

# Direct imaging of nanoscale field-driven domain wall oscillations in Landau structures†

Balram Singh, [ID] [a,b] Rachappa Ravishankar, [ID] [a] Jorge A. Otálora,[c] Ivan Soldatov,[a] Rudolf Schäfer,[a,d] Daniil Karnaushenko,*[e] Volker Neu [ID] *[a] and Oliver G. Schmidt*[b,e,f]

Linear oscillatory motion of domain walls (DWs) in the kHz and MHz regime is crucial when realizing precise magnetic field sensors such as giant magnetoimpedance devices. Numerous magnetically active defects lead to pinning of the DWs during their motion, affecting the overall behavior. Thus, the direct monitoring of the domain wall's oscillatory behavior is an important step to comprehend the underlying micromagnetic processes and to improve the magnetoresistive performance of these devices. Here, we report an imaging approach to investigate such DW dynamics with nanoscale spatial resolution employing conventional table-top microscopy techniques. Time-averaged magnetic force microscopy and Kerr imaging methods are applied to quantify the DW oscillations in $Ni_{81}Fe_{19}$ rectangular structures with Landau domain configuration and are complemented by numeric micromagnetic simulations. We study the oscillation amplitude as a function of external magnetic field strength, frequency, magnetic structure size, thickness and anisotropy and understand the excited DW behavior as a forced damped harmonic oscillator with restoring force being influenced by the geometry, thickness, and anisotropy of the $Ni_{81}Fe_{19}$ structure. This approach offers new possibilities for the analysis of DW motion at elevated frequencies and at a spatial resolution of well below 100 nm in various branches of nanomagnetism.

## Introduction

Investigation of the domain wall (DW) oscillation behavior has provided deep insight in various areas of applied magnetism, *e.g.*, the understanding of the giant magneto-impedance effect,[1–4] the dynamic magnetization processes relevant to minimize core losses in soft magnetic electrical transformer sheets[5–8] and the functionality of magnetophoretic devices based on DW motion.[9–13] Maximum velocity, mobility, mass, pinning and linearity of a DW motion are properties of major relevance in the responsiveness of DW based sensors and devices. The first three properties have been mainly studied by

imaging the DW displacement after applying a dc-bias pulse,[14–19] and by selected experiments on probing the resonance frequency of a pinned DW,[20–23] but there is a lack of information on the real-time behavior of an ac-excited DW, including effects of pinning and linearity, due to limits in the state of the art of experimental techniques to characterize the precise *in situ* movement of a DW. Hence, development of a high spatial resolution imaging method to investigate the trajectory of the ac-excited DW is important for advancing magnetic sensor technology[24] as well as for understanding fundamental DW properties.

The response of a domain wall or vortex to high frequency (>MHz) ac-excitations has been studied employing time-resolved imaging using X-ray-,[22,25,26] Lorentz-[27] and Kerr microscopy.[28–30] However, imaging the trajectory of a domain wall with a time-resolved technique is an extremely challenging task. Additionally, imaging with the first two microscopy techniques requires X-ray- or electron beam-transparent substrates, and Kerr microscopy is limited by its moderate resolution in the micrometer range. In the kHz frequency region and below, DW dynamics has been explored by measuring the complex permeability (an *averaged* property of the sample) by means of the magneto-optical Kerr effect (MOKE)[31–33] and by magnetoimpedance measurements.[4,34–36] In this approach, DW velocities and mobilities are extracted from the measured permeability as a function of excitation field amplitude and frequency.

[a]*Institute for Integrative Nanosciences, Leibniz IFW Dresden, 01069 Dresden, Germany. E-mail: v.neu@ifw-dresden.de*

[b]*Nanophysics, Faculty of Physics, TU Dresden, 01062 Dresden, Germany*

[c]*Departamento de Física, Universidad Católica del Norte, Avenida Angamos 0610, Casilla 1280, Antofagasta, Chile*

[d]*Institute for Materials Science, TU Dresden, 01062 Dresden, Germany*

[e]*Center for Materials, Architectures and Integration of Nanomembranes (MAIN), Chemnitz University of Technology, 09126 Chemnitz, Germany.*
*E-mail: oliver.schmidt@main.tu-chemnitz.de,*
*daniil.karnaushenko@main.tu-chemnitz.de*

[f]*Material Systems for Nanoelectronics, Chemnitz University of Technology, 09107 Chemnitz, Germany*

†Electronic supplementary information (ESI) available. See DOI: https://doi.org/10.1039/d2nr03351h

When it comes to resolving nanoscale domain features, magnetic force microscopy (MFM) has proven to be a very powerful technique,[37,38] that is however, largely unexplored concerning imaging of time-dependent domain processes. Few reports are the early measurements of the write head fields in the MHz regime[39–41] and the more recent development of side-band MFM.[42] In both cases, MFM is used for a successful mapping of temporal field dynamics, but not for imaging oscillatory spatial DW processes.

In this work, we developed two direct imaging methods based on conventional table-top magnetic force microscopy (MFM) – real-time and time-averaged imaging to investigate the DW's oscillation trajectory in the range of millihertz (mHz) and kilohertz (kHz) frequencies, respectively. We take advantage of MFM's high spatial resolution and quantify the DW dynamic oscillation amplitude down to 60 nm and thus eliminate the need of challenging time-resolved imaging methods, special sample preparation and complex equipment. To extend our studies to larger oscillation amplitudes, time-averaged imaging using Kerr microscopy is performed. In that Kerr imaging approach, valuable information can be obtained by regular difference-image processing,[43] which is robust, easy and fast to perform.

In the case of real-time MFM imaging, the MFM tip records the DW position in quasi-static mode, as in that case DW moves rather slowly (frequency of few tens of mHz) in comparison to the tip's scan speed (frequency of a few Hz).

The basic principle of the second imaging method, i.e., time-averaged MFM imaging, is summarized in Fig. 1. In case of a static DW (Fig. 1a1), the DW's spatial position does not change with time, so the dwell time function of the DW, $t_D$, i.e. the time spent by the domain wall at a given position, peaks at the static DW position (Fig. 1b1). For a sinusoidally excited DW (Fig. 1a2 and a3), the periodicity of ac excitation strictly defines the DW position ($\propto B$) and DW velocity ($\propto dB/dt$). Due to the position-dependent DW velocity, the dwell time function (Fig. 1b2 and b3) depends on the position of the DW with respect to its static position. For DW oscillation frequencies (in kHz) much higher

than the MFM tip's scan speed (0.1 Hz), the DW interaction felt by the tip is averaged at a given position and therefore scales with the dwell time $t_D$. The MFM signal thus contains the corresponding information of the DW oscillation's trajectory and amplitudes. Using these imaging methods, together with a quantitative analysis, we studied the DW dynamics of soft ferro-magnetic permalloy rectangles in the Landau domain configuration as a function of excitation strength, frequency, structure size, thickness and strain induced magnetic anisotropy (along the long axis) of the rectangle. Soft ferromagnetic permalloy ($Ni_{81}Fe_{19}$) rectangles have been chosen due to the well-known Landau structure ground state (with stable 180° domain wall) and the material's high permeability,[44] which is therefore suit-able for periodic domain wall dynamics.

## Results and discussion

### MFM imaging

In MFM, the oscillating cantilever detects the force derivative $\partial F_z/\partial z$ originating from the magnetostatic interaction between the tip's magnetic coating and the sample's stray field, in our case that of the 90° and 180° Néel and cross-tie domain walls of the Landau pattern as shown in Fig. 2a. Further details such as a periodic contrast variation along the 180° wall are dis-cussed in the ESI, Fig. S1 and ESI Note 1.† Prior to measuring fast DW oscillations above 100 Hz in the time-averaged regime, we directly imaged the quasi-static real-time motion of a slowly moving DW at 0.01 Hz. In both cases, the translational sym-metry of the 180° DW along the $y$-axis and the DW movement along the $x$-axis allow disabling the slow scan axis ($y$-axis) without loss of information. In this mode, the image's $y$-axis actually corresponds to a time-axis, clocked by the scan rate of the cantilever.

**Real-time MFM imaging of slow periodic DW motion.** With the slow scan axis disabled (for details see ESI, Fig. S1 and ESI Note 1†), the periodic domain wall oscillations were imaged in real-time (Fig. 2b) by applying an ac-magnetic field of ampli-
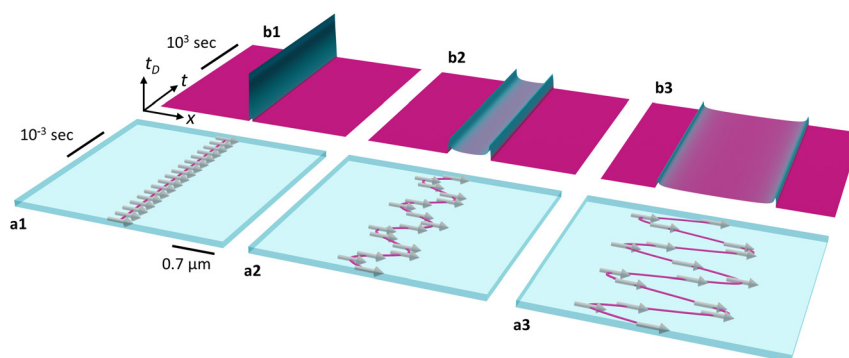


**Fig. 1** Concept of time-averaged MFM imaging of DW oscillations. (a) Schematics of a static and oscillating Néel type domain wall in the $x$–$t$ (posi-tion–time) plane for zero and two non-zero oscillation amplitudes. The magenta color line together with the magnetic moment vectors parallel to the surface in images a1–a3 illustrate the Néel type DW center. The DW position is sketched as a function of time for the static case (a1) and the dynamic case at a frequency of 1 kHz with amplitude 0.3 μm (a2) and 0.76 μm (a3). (b) Normalized dwell-time $t_D$ for static (b1) and oscillating DW with amplitude 0.3 μm (b2) and 0.76 μm (b3). Note the different time-scales in panels (a) and (b).
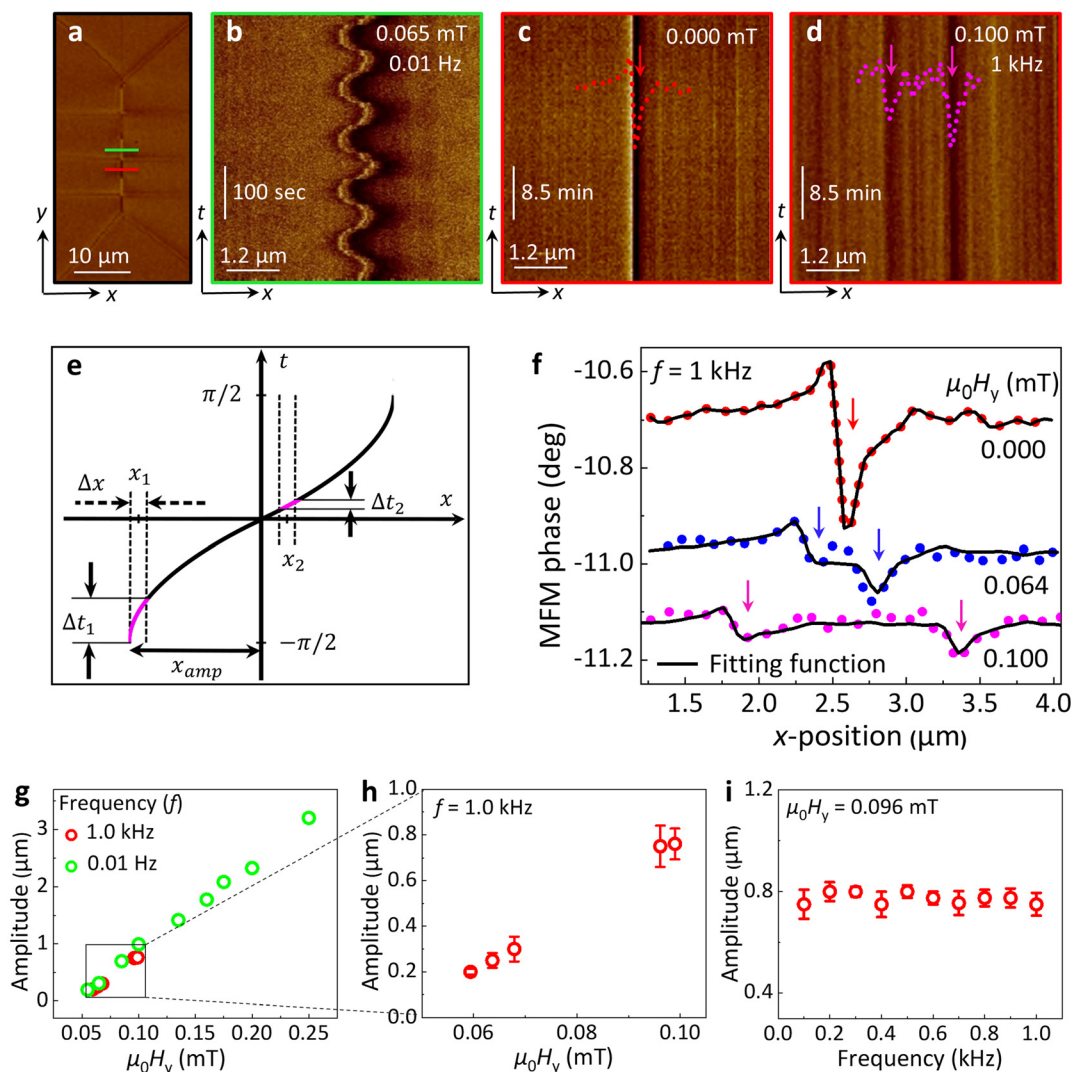
**Fig. 2** Real-time and time-averaged MFM imaging of domain wall oscillation in a permalloy Landau structure ($L = 50$ μm, $W = 25$ μm, $d = 50$ nm). (a) Demagnetized state of the permalloy rectangle in the MFM $x$–$y$ scanning mode, with two colored solid lines indicating the positions imaged with slow-scan axis disabled in the following measurements (see colored frames of panel b – d). (b) Real-time imaging of the quasi-static domain wall oscillating with 0.01 Hz ($\mu_0 H_{ac} = 0.065$ mT) in the $x$–$t$ plane, imaged with slow-scan axis disabled. (c) Static DW in the $x$–$t$ plane, imaged with the slow-scan axis disabled. The intensity profile across the DW is shown as a red dotted line and the arrow indicates the DW position. (d) Time-averaged imaging of the DW oscillating with a frequency of 1 kHz ($\mu_0 H_{ac} = 0.10$ mT) in the $x$–$t$ plane, imaged with slow-scan axis disabled. (e) Sketch of sinusoidal domain wall oscillation, illustrating the magnitude of the dwell time (magenta color region) at two different pixel positions. (f) Measured intensity profiles of the static DW and the time-averaged DW oscillating at 1 kHz (dotted lines). The solid lines show the analytical function used to fit the experimental data (see main text). The arrows indicate the fixed DW position at zero field and the two extreme positions in case of an oscillating DW. (g) DW oscillation amplitude as a function of the ac-field amplitude. (h) Magnified view of (g) for 1 kHz frequency data. (i) DW oscillation amplitude as a function of excitation frequency for constant ac-field amplitude.

tude 0.065 mT and frequency $f = 0.01$ Hz along the long ($y$-) axis of the rectangle. With a cantilever scan rate of 1.0 Hz (along the fast scan axis, *i.e.,* the $x$-axis), which is 100 times faster than the domain wall oscillation frequency, each scan line in the MFM image records the profile of the quasi-static DW with the DW position depending on the momentary field value. The sinusoidal DW oscillation is thus directly seen in the recorded MFM image with an oscillation period $T = 100$ s and the peak-to-peak oscillation amplitude can be simply extracted from the displacement in the line scans that corres-

pond to opposite return points. As expected, the oscillation amplitude $x_{amp}$ (*i.e.* half of the peak-to-peak amplitude) varies linearly with the peak ac-field amplitude $\mu_0 H_y$ (Fig. 2g, green open symbols).

**Time-averaged MFM imaging of fast periodic DW motion.** At higher ac-field frequencies (above 0.1 Hz), the DW's periodic motion becomes faster and competes with the scan speed. Thus, simple real-time imaging starts to fail. For frequencies above 100 Hz, a time-averaged imaging technique is applied to capture the oscillations. Fig. 2c and d display the MFM phase

contrast (imaged by keeping the 'slow scan axis' disabled) of the static and dynamically oscillating DW, respectively. With a cantilever scan rate of 0.1 Hz (along the fast $x$-scan axis), which is $10^4$ times smaller than the DW oscillation frequency (1 kHz), even within the acquisition time of one pixel the DW performs several periods of motion. The MFM tip thus senses the time-averaged phase change signal proportional to the time that the DW is present at that position. In the case of a sinusoidal DW oscillation, due to position dependent DW velocities, this so-called dwell time is also position dependent and consequently the longest tip-DW interaction appears as two darker vertical lines at the return points (or amplitude) of the DW oscillation (Fig. 2d). The intensity profile of this measurement (obtained by averaging the line contrast along the $y$-axis) is superposed onto the image as a magenta dotted line. The two minima in the intensity signal represent the peak positions of the oscillating DW. This intensity profile is furthermore plotted in Fig. 2f together with a measurement at $\mu_0 H_y = 0.064$ mT (blue dotted line) and zero excitation field (red dotted line). The signal from the static DW presents the regular MFM interaction between the magnetic tip and the DW stray fields. As the excitation amplitude becomes non-zero, the DW signal first becomes broader (shown in ESI, Fig. S2 and ESI Note 2†) and then splits into the observed two minima. If the excitation amplitude is further increased, the peak positions move further apart and the minima become shallower.

For a quantitative analysis of such an intensity profile the dwell time is derived as a function of DW position along the $x$-direction according to Fig. 2e, where DW oscillations are assumed to be purely periodic and sinusoidal. Periodicity of the process is assumed on the basis of the periodic excitation. For a certain position $x_i$ along the scan line, the DW contributes to the signal when it stays at this position $x_i$ within the limits of the pixel size $\Delta x$. This is illustrated in Fig. 2e for two positions $x_1$ and $x_2$. At position $x_1$, close to the return point of the DW, dwell time is significantly longer whereas at $x_2$, close to the equilibrium position, the fast moving DW causes the tip to only briefly interact with the DW within the pixel acquisition time. The dwell time, $t_D$ is expressed as

$$t_D(x) = [\sin^{-1}(b/x_{amp}) - \sin^{-1}(a/x_{amp})]/\pi \quad (1a)$$

which is normalized by the period of oscillation $T$. $x_{amp}$ is the peak amplitude of the DW oscillation and the limits, $a$ and $b$, are given by

$$a = \max(x - \Delta x/2, -x_{amp}); \quad b = \min(x + \Delta x/2, -x_{amp}). \quad (1b)$$

As the MFM contrast of a magnetic object is necessarily broadened, the MFM signal recorded from the oscillating DW is finally the convolution[45] of the static MFM profile with the above normalized dwell time function:

$$\text{MFM}_{ac}(x) = \text{MFM}_{static}(x) \otimes t_D(x; x_{amp}) \quad (2)$$

The solid black lines in Fig. 2f are the convolved signals (using eqn (2)), based on the measured static MFM profile and

with only the oscillation amplitude $x_{amp}$ as a free fitting parameter. Details on the intensity model and the fitting procedure are given in the ESI, Fig. S3 and ESI Note 3.† Apparently, all experimental features are well described by the model, confirming the assumptions of periodicity, sinusoidal DW movement and the ansatz of a time-averaged phase shift signal. The oscillation amplitude $x_{amp}$ as a function of $\mu_0 H_y$ is seen in Fig. 2h as a separate panel and in Fig. 2g together with the quasi-static data, in good agreement despite the largely different excitation frequencies. Besides confirming the linear increase of $x_{amp}$ with $\mu_0 H_y$, these measurements in the small field regime allow a precise determination of the depinning field $H_p$ from the intercept with the abscissa. Below a value of $\mu_0 H_p = 0.05$ mT, DW movement is suppressed due to pinning, supposedly mainly caused by pinning of the Blochlines which occur at the cross-tie walls. As seen from Fig. 2i, the excitation frequency has almost no influence on the oscillation amplitude at fixed field amplitude ($\mu_0 H_y = 0.096$ mT). An inherent feature of the time-averaged signal for sinusoidal oscillations is that the signal strength continuously decreases with increasing oscillation amplitude. The time-averaged MFM approach can thus best be used under the following conditions: (i) oscillation amplitudes at or below the micrometer range, where one can also take advantage of the high MFM resolution; (ii) large static DW signal for good signal-to-noise ratio; (iii) magnetic materials with low pinning and easy domain wall movement for an instantaneous relaxation into the field dependent equilibrium position.

### Time-averaged Kerr imaging

In order to extend the DW dynamics study to larger DW oscillation amplitudes, we performed time-averaged imaging by Kerr microscopy. Fig. 3a shows the Landau pattern in the zero field state,[46] which was obtained after an ac-field demagnetizing procedure. The bright and dark areas in Fig. 3a resemble the magnetic domains, aligned parallel and anti-parallel to the long axis. Additional weak contrast within these domains arises from the cross-tie walls, which are expected for permalloy films with the given thickness. The imaging of DW oscillations was performed with a typical exposure time of 6.4 s (i.e., multiple oscillations within that time are averaged), with an image of the original zero-field Landau state (Fig. 3a) being subtracted. A typical difference image, obtained by that procedure for a field amplitude of 0.40 mT and a frequency of 1 kHz, is shown in Fig. 3b.

In the dynamically averaged difference image (i.e., time-averaged image obtained after background subtraction and ac-field application, Fig. 3b), due to DW motion the domain areas that do not grow or shrink, stay gray, while parts with alternating magnetization show up as contrast. A bright difference contrast to the right side is the result of the growing bright domain during the positive cycle of excitation. Similarly, the dark contrast to the left side is the result of the growing dark domain during the negative cycle of excitation. Thus, the change of contrast contains information about the DW movement and especially its maximum displacement
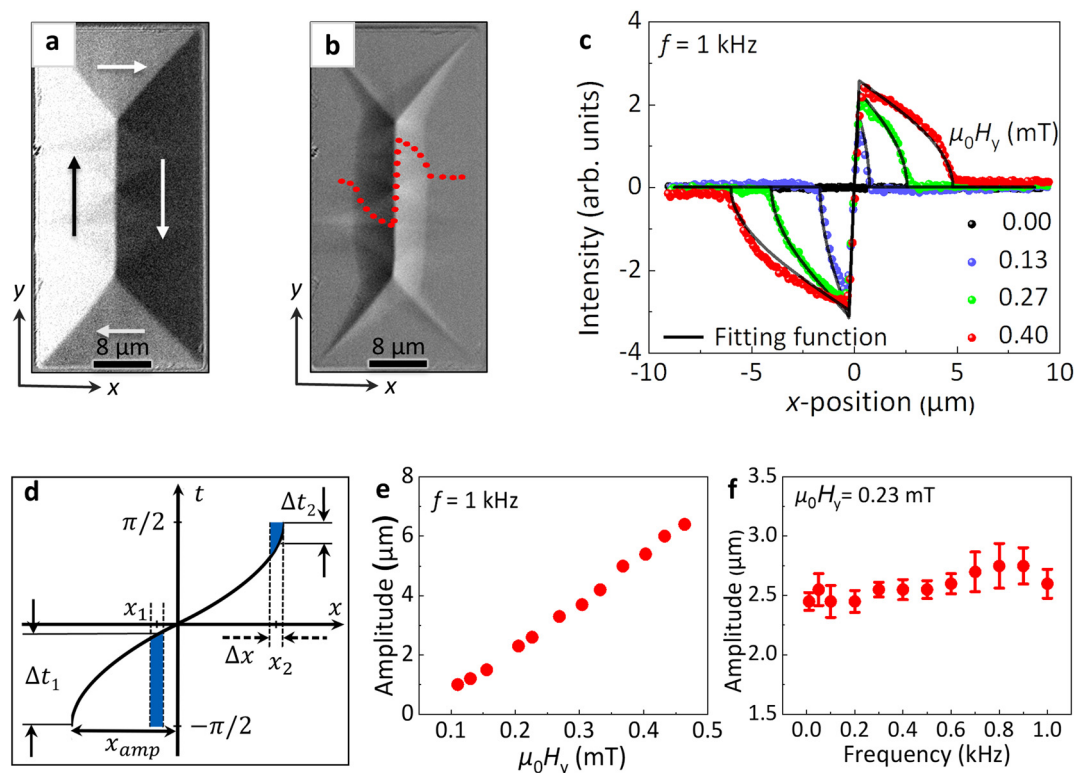
**Fig. 3** Time-averaged Kerr imaging for the study of magnetic domain wall oscillation in the same permalloy element as in Fig. 2. (a) AC-demagnetized state of the permalloy rectangle. (b) Dynamically averaged difference image of the domain walls oscillating at a frequency of 1 kHz ($\mu_0 H_y$ = 0.40 mT); the red dotted line shows the intensity profile (line scan) of the oscillating 180° domain wall. (c) Measured intensity profile of the dynamically averaged difference images for different DW oscillation amplitudes at 1 kHz (colored symbols). The solid black lines are fits to the experimental data (see text). (d) Sketch for sinusoidal domain wall oscillation, with the magnitude of the shaded areas indicating the average amount of time spent by the expanding domain (due to DW motion) at two different $x$-positions. (e) DW oscillation amplitude *vs.* field amplitude at a constant excitation frequency of 1 kHz. (f) DW oscillation amplitude as a function of excitation frequency at fixed field amplitude of $\mu_0 H_y$ = 0.23 mT.

when subjected to an ac-magnetic field. Additional superimposed contrast is coming from the cross-tie walls. The intensity profile across the 180° DW is superposed onto the image. Such intensity profiles of dynamically averaged difference images captured at different excitation field values (at a constant excitation frequency of 1 kHz) are plotted as solid colored symbols in Fig. 3c. The intensity at a given position on the $x$-axis scales with the average time the magnetic domain extended beyond that position during the oscillation. This is illustrated in Fig. 3d, where the sinusoidal DW movement is plotted in a time-position diagram and the respective time (dwell time) is sketched as a blue line for two different positions $x_1$ and $x_2$. Obviously, at position $x_1$ close to the equilibrium ($x = 0$), the DW spends a large time interval $\Delta t_1$ beyond $x_1$, while at $x_2$ (close to the return point) the DW enters the region at and beyond $x_2$ only during a short time interval $\Delta t_2$ where it contributes to the measured difference image. Apart from being determined by the length of the time interval, the intensity changes also sign with the sign of $x$. Furthermore, due to the spatial extension of the DW signal (given by the optical resolution $\Delta x$), the intensity is given by

the integral across the resolution width of the sign-weighted dwell time.

$$\text{Intensity}(x) = C \cdot \int_a^b \left[ (\pi/2) \cdot \text{sign}(x) - \sin^{-1}(x/x_{\text{amp}}) \right] \mathrm{d}x \quad (3a)$$

where $\text{sign}(x)$ is the sign function, $C$ a scaling factor, and $x_{\text{amp}}$ the peak amplitude of the DW oscillation. The integration limits depend on the DW position $x$ and are defined as

$$a = \max(x - \Delta x/2, -x_{\text{amp}}); \quad b = \min(x + \Delta x/2, x_{\text{amp}}) \quad (3b)$$

identical to their definitions in (1b).

The intensity profiles calculated according to eqn (3a), are fitted to the experimental data by adjusting the oscillation amplitude $x_{\text{amp}}$ while keeping $C$ and $\Delta x$ fixed for a given set of data. Details on the intensity model and the fitting procedure are given in the ESI, Fig. S4 and ESI Note 4.† The very good match between the measured and the modeled signal confirms the sinusoidal DW movement and provides a robust evaluation of $x_{\text{amp}}$. Results for varying field amplitudes and excitation frequencies are summarized in Fig. 3e and f,

respectively. The DW oscillation amplitude increases linearly with the field amplitude $\mu_0 H_y$, while it displays no significant dependence (within the error bars) on the excitation frequency in the studied range from 100 Hz to 1 kHz. With respect to the magnetooptical signal detection, the time-averaged measurement approach involves no upper limit concerning the DW oscillation amplitude and frequency, however, we are limited to excitation frequencies of 1 kHz due to restrictions of the power supply and the inductance of the field coils.

Our observations indicate that even at $f_{ac}$ = 1 kHz the DW is still instantaneously following the excitation field. Studies performed by Kerr susceptometry on $Co_2MnGe$[33] and Co[32] stripes report dependencies of the DW oscillation amplitude on both, excitation amplitude and frequency. For a fixed excitation amplitude, the DW oscillation amplitude varies with excitation frequency. For instance, at a field value close to the coercive field of the magnetic structure, the DW oscillation amplitude starts to decrease above a cutoff frequency (which is around 28–38 Hz and 1500–3700 Hz, depending on the field value applied in $Co_2MnGe$ and Co stripes, respectively) and reduces to zero on further increase in excitation frequency. The cutoff frequency is linked to the DW mobility, which is deduced from the experiment to be 11 m s$^{-1}$ mT$^{-1}$ for the 60 nm thick $Co_2MnGe$ film and 150 m s$^{-1}$ mT$^{-1}$ for the 40 nm thick Co film. These results suggest, that in our 50 nm thick permalloy structures, for which a DW mobility around 100 m s$^{-1}$ mT$^{-1}$ is expected,[47,48] the DW amplitudes up to 1 kHz excitation frequency should not decay with frequency, which agrees with the experimental observation. It further indicated, that the DW dynamics in permalloy rectangles in the applied field and frequency range occurs in the flow regime.

### Influence of structure size and thickness: experiments

To develop a better understanding of the DW dynamics in permalloy rectangles, two additional rectangles of different dimensions were prepared, and the DW dynamics was analyzed by means of the time-averaged MFM and Kerr imaging

(Fig. 4). Compared to the structure (rectangle 1) with edge length $L$ = 50 μm and permalloy thickness $d$ = 50 nm (discussed so far), rectangle 2 has a film thickness of $d$ = 20 nm. Rectangle 3 maintains the thickness of 20 nm but with a reduced edge length of $L$ = 30 μm (microscopic images of rectangles 2 and 3 are shown in ESI, Fig. S1†). After ac-demagnetization, rectangles 2 and 3 reveal the Landau ground state with 180° domain walls, but without crossties, in agreement with the reduced thickness.[46] According to Fig. 4a, the geometry has a decisive effect on the oscillation amplitude,[49,50] with a strong increase in $x_{amp}$ with decreasing film thickness (compare rectangle 1 and 2) and a strong decrease in $x_{amp}$ for reduced planar dimensions (compare rectangle 2 and 3). The depinning fields for the thin rectangles 2 and 3 are similar ($\mu_0 H_p \cong 0.02$ mT) and smaller than for rectangle 1 ($\mu_0 H_p \cong 0.05$ mT). Concerning the dynamic behavior, the oscillation amplitude is independent of excitation frequency up to 1 kHz, as seen in Fig. 4b measured by MFM and Kerr microscopy for rectangles 1 and 3 at two different excitation field amplitudes $\mu_0 H_y$.

A simple argument for the increasing amplitude $x_{amp}$ with increased edge length $L$ is as follows: a given field $\mu_0 H_y$ applied to the permalloy rectangle will roughly lead to the same normalized net magnetization $m_y$, irrespective of the structure size. Thus, the structure with larger width ($W = L/2$) will allow a larger absolute DW displacement.[49,50] This, however, cannot explain the increase in $x_{amp}$ with decreasing film thickness $d$. A full explanation needs to consider the true magnetization configuration and its energy terms, including the demagnetization energy and exchange energy contained in the field-dependent domain pattern and the domain walls.

### Influence of structure size and thickness: micromagnetic simulation

The quasi-static DW dynamics was simulated by performing numeric micromagnetic simulations in permalloy rectangles. To study the influence of structure size and thickness on DW
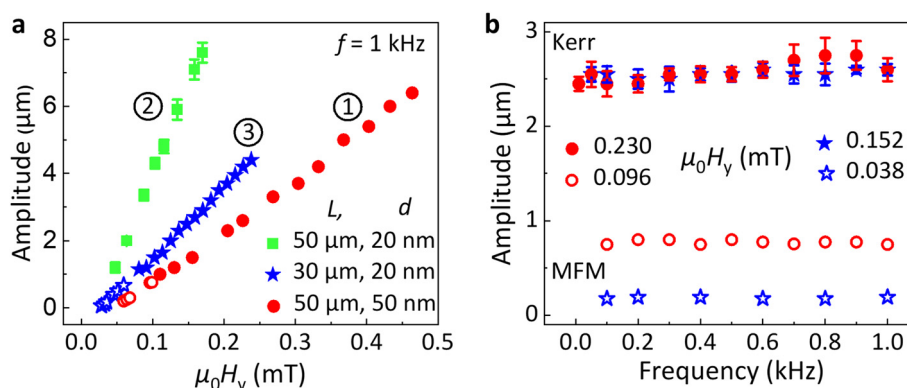


**Fig. 4** Comparison of domain wall oscillation amplitude in rectangles of different geometry imaged by MFM (open symbols) and Kerr microscopy (solid symbols). (a) DW oscillation amplitude *vs.* field amplitude at a constant frequency of 1 kHz for three different rectangles. *L* and *d* denote length and thickness of rectangle keeping the length to width (*W*) aspect ratio constant at *L*/*W* = 2 : 1. Rectangle 1 is the permalloy element discussed in Fig. 2 and Fig. 3. (b) DW oscillation amplitude *vs.* frequency at constant field value for rectangle 1 and 3 (for labels see panel (a)).

dynamics, simulations are performed starting from rectangles with dimensions almost 10 times smaller (due to limitations in computing power) up to the dimensions of the smallest experimentally realized rectangle (rectangle 3). The chosen dimensions for simulation are sufficiently large to replicate the experimental observed domain configuration, except for the cross-tie walls, which are absent also in the thickest (52 nm) simulated rectangle. For analyzing DW dynamics, magnetic domain configurations were obtained at different applied fields $\mu_0 H_y$, and the DW displacement was analyzed. When staying below a net magnetization $m_y < 0.5$, the amplitude (displacement) increased linearly with $\mu_0 H_y$, as observed in the experiments (shown in ESI, Fig. S5a and b†). The DW displacement at a constant field $\mu_0 H_y = 0.1$ mT is plotted as a function of edge length $L$ and thickness $d$ in Fig. 5a and b, respectively. In Fig. 5a, simulations were performed for permalloy structures with 20 nm thickness and edge lengths $L$ from ranging from 3.7 μm to 30 μm, and the displacement (amplitude) clearly increases with $L$ as also seen in the experiment. The data can be described by a power law $x_{amp} \propto L^p$, with an exponent $p = 2.09$. Due to limited computer memory it was not possible to perform the simulations for $L = 50$ μm and thus the fitted power law was extrapolated to 50 μm length (red solid line in Fig. 5a). In Fig. 5b, simulations

are summarized for rectangles of fixed size ($L = 5.6$ μm) but various thicknesses between 12 and 52 nm. As observed in the experiment, the DW displacement for a fixed field decreases with thickness. The data can be described by an inverse power function $x_{amp} \propto d^{-p}$, with exponent $p = 0.81$. Besides this qualitative comparison, which confirms the observed dependency on the pattern geometry, the simulations displayed in Fig. 5a also allow a direct quantitative comparison with the experiment. The experimentally determined dynamic amplitudes $x_{amp}$ at $f = 1$ kHz for the two 20 nm thick rectangles with $L = 30$ μm and 50 μm are included in the graph and match the static simulations well (maximum error of 7.5%). This again corroborates, that the DW instantaneously follows the externally applied field, and that apart from the small effect of the depinning field the DW displacement in this frequency range is not influenced by details of the microstructure of the material. This is certainly a consequence of the 'self-sustaining' domain configuration of the Landau pattern, where the equilibrium position in a given field is determined solely by the gain in Zeeman energy *versus* the costs of an increased exchange and demagnetization energy. With an appropriate estimation of the latter, a simple energy approach can lead to a complete description of the studied domain structure.
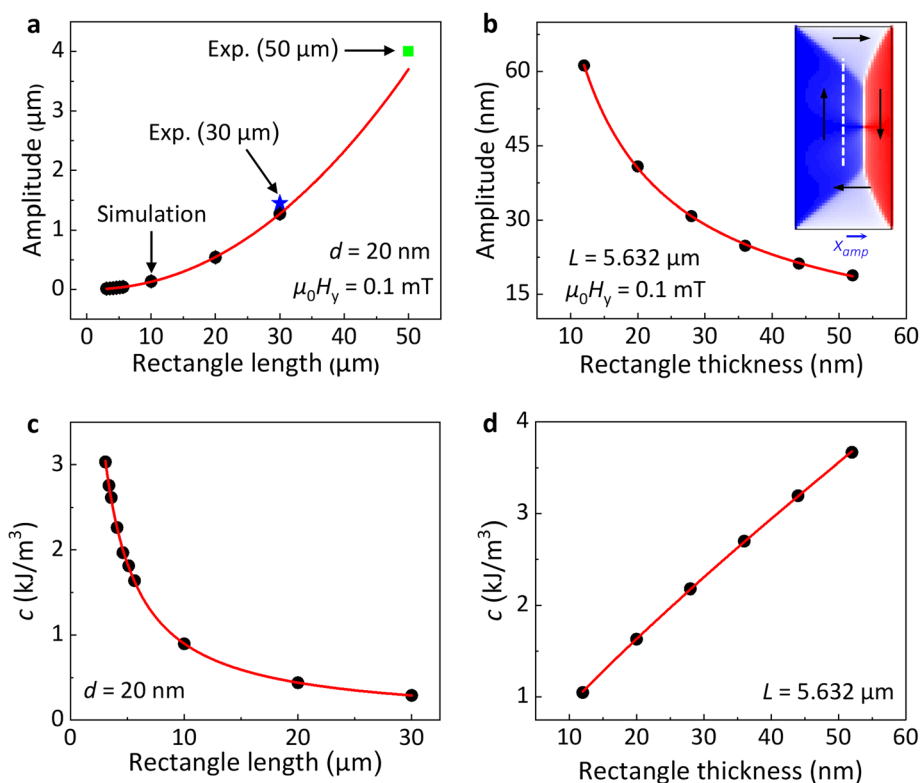


**Fig. 5** Micromagnetic OOMMF simulation of quasi-static DW dynamics for permalloy rectangles of different geometry. (a) DW oscillation amplitude *vs.* length of the rectangle (keeping aspect ratio 2:1 and thickness 20 nm constant). The green square and blue star symbols denote the experimental data for rectangle of lengths 50 μm and 30 μm (thickness 20 nm). (b) DW oscillation amplitude *vs.* thickness of rectangle (keeping length constant). Simulated permalloy rectangle in inset shows equilibrium magnetic domain states with displaced DW (to magnitude $x_{amp}$) in the presence of a field along the rectangle's long axis. (c) Stiffness parameter $c$ (acquired from average energy density (Exchange + Demag) *vs.* $m_y$) as a function of rectangle length. (d) Stiffness parameter $c$ as a function of rectangle thickness. The red solid lines show fits to the simulated data.

For that, the sum of demagnetizing energy and exchange energy was extracted from the micromagnetic simulations as a function of $m_y$ for small external fields around zero (see ESI, Fig. S5c and d†). In all simulations, a quadratic increase in energy density with $m_y$ was observed, which can be expressed as

$$\varepsilon_{ex+demag} = c_0 + c \cdot m_y^2 \qquad (4)$$

where the stiffness parameter $c$ quantifies the restoring force on the DW when displaced from the equilibrium position with $m_y = 0$. This parameter is plotted in Fig. 5c as a function of edge length $L$ and shows a hyperbolic decay according to $c \propto L^{-1.03}$. The corresponding analysis for varying film thickness is displayed in the Fig. 5d and leads to a stiffness parameter $c \propto d^{0.84}$, varying roughly linearly with thickness.

The equilibrium DW position, $x_{amp}$, is then derived from minimizing the total energy density (see ESI, Note 5†), and reads:

$$x_{amp} = \frac{\mu_0 M_s}{8\beta} \cdot \frac{L}{c} \cdot H \qquad (5)$$

The factor $\beta$ corrects for the closure domains with transverse magnetization. This final expression (eqn (5)) contains the linear dependence of $x_{amp}$ on $H$, and also an explicit linear dependence on the edge length $L$, which we discussed already with the experimental observation. The details of the geometry are contained in the stiffness parameter $c$. The hyperbolic decay $c \propto L^{-1.03}$ largely explains the numerically observed dependency $x_{amp} \propto L^{2.09}$. Likewise, the thickness dependence $x_{amp} \propto d^{-0.81}$ is understood from $c \propto d^{0.84}$.
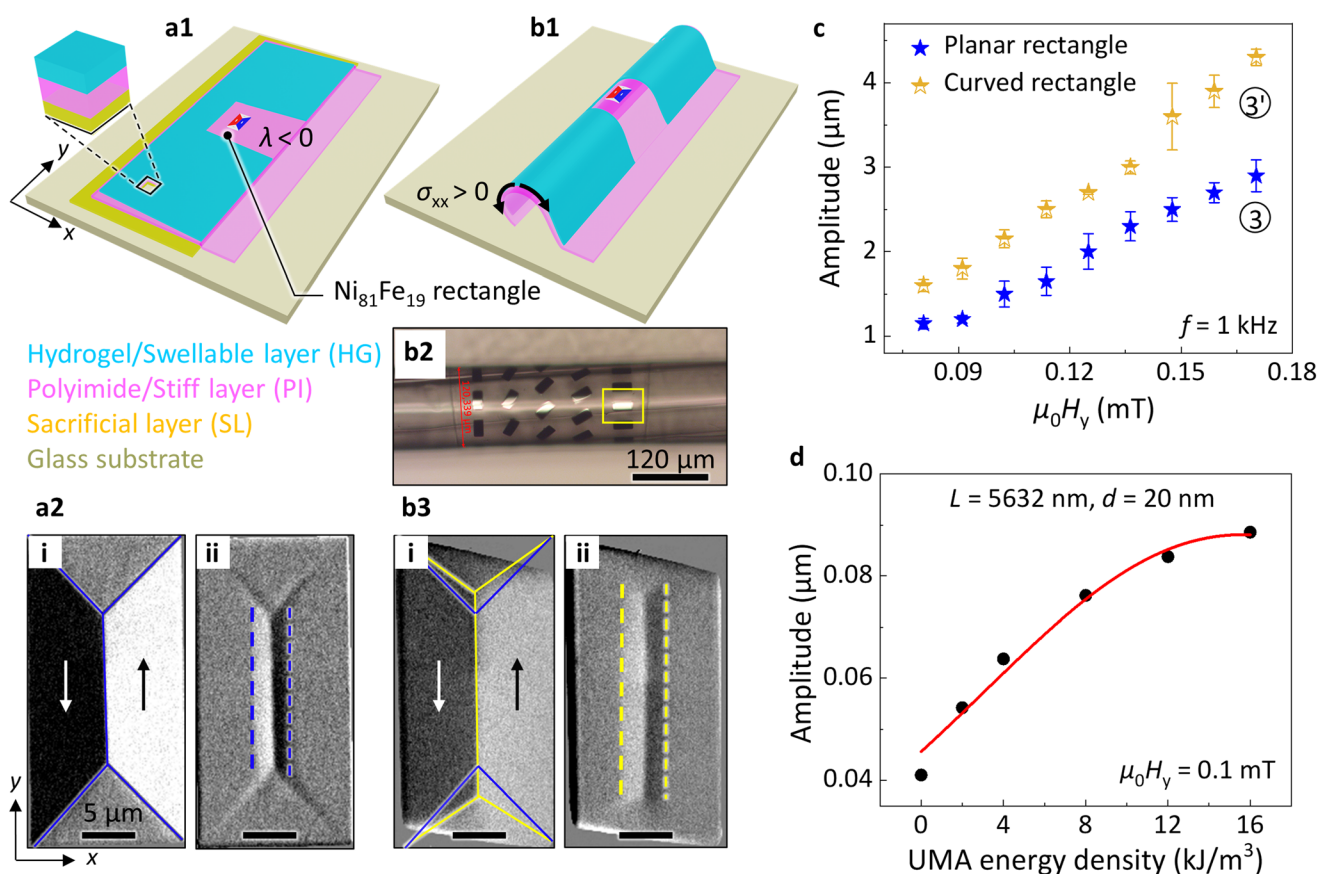


**Fig. 6** Influence of induced uniaxial magnetic anisotropy on DW oscillation amplitude of permalloy rectangle. (a1 and b1) Schematic images of the polymeric platform (PP) with the magnetic rectangle placed on top of the polymeric platform before rolling (a1), and after self-assembled roll-down (b1). The absence of a hydrogel (HG) layer in the central region is for placing the magnetic structure. The black arrows show the stress direction in the magnetic structure. (b2) Optical image of polymeric platform after self-assembly rolling-down with magnetic structures placed on it. The structure inside the yellow box is the studied permalloy rectangle 3 ($L = 30$ μm, $W = 15$ μm, $d = 20$ nm). Kerr images of static domains, (a2-i) before rolling and (b3-i) after rolling down. The black and white arrows show the domain orientation. The solid blue (before rolling, a2-i) and yellow lines (after rolling, b3-i) are used to guide to the domain wall positions. Time-averaged Kerr images of DW oscillations with field applied along $y$-axis ($\mu_0 H_y = 0.125$ mT, $f = 1$ kHz) before rolling (a2-ii) and after roll-down (b3-ii). The dotted blue and yellow lines indicate the DW oscillation amplitudes. Deformation seen at the short edges of the Kerr images of the rolled structure appears due to imaging of a curved surface. (c) Comparison of DW oscillation amplitude (at $f = 1$ kHz) before and after rolling the rectangle. (d) Micromagnetic OOMMF simulation of DW oscillation amplitude in permalloy rectangle ($L = 5632$ nm, $W = 2816$ nm, $d = 20$ nm) at 0.1 mT with increasing uniaxial magnetic anisotropy energy density $K_u$ (along the long-axis of the rectangle). The red solid line shows a fit to the simulation data (for detailed information see ESI, Note 7†).

## Influence of magnetic anisotropy: experiments and micromagnetic simulations

An additional energy density term that plays an important role in DW dynamics is the uniaxial magnetic anisotropy (UMA). It can be induced in a soft ferromagnetic material by several means.[51–54] In this work, we induce a UMA parallel to the long axis of the permalloy rectangle by depositing the element on a recently developed shapeable polymeric platform for controlling sign and magnitude of the elastic strain.[51] A polymeric platform stack of sacrificial layer (SL), polyimide layer (PI) and hydrogel layer (HG) is prepared (Fig. 6a1), where the hydrogel (HG) will swell in an alkaline solution against the retaining force of the PI. This will lead to a rolling down of the polymer platform, once it is released from the substrate by etching the SL (Fig. 6b1 and b2). The 20 nm thick permalloy on top experiences a positive (tensile) stress ($\sigma > 0$) along the rolling direction, *i.e.* perpendicular to the rectangle's long axis (see ESI, Fig. S6 and ESI Note 6†). With a residual negative magnetostriction ($\lambda < 0$) value of $Ni_{81}Fe_{19}$ and according to the equation of magnetoelastic energy constant,[55] $K_u = (3/2)\sigma\lambda$, the strain-induced uniaxial anisotropy is negative and thus lies perpendicular to the strain direction, *i.e.*, along the long rectangle edge. In the unrolled state the rectangle reduces the magnetostatic energy by conforming to the shape of the structures,[56] *i.e.* by forming the already discussed Landau pattern (Fig. 6a2-i). After being self-assembled in a roll-down fashion, the Kerr image Fig. 6b3-i shows an increase of the area of the already existing domains oriented along the long axis, and thus parallel to the induced UMA. The DW dynamics was analyzed by means of the time-averaged Kerr imaging technique.

The increase in oscillation amplitude after rolling is immediately visible by comparing the time-averaged dynamic difference images to those of the unrolled structure (Fig. 6a2-ii and b3-ii). A quantitative comparison for several field amplitudes is shown in Fig. 6c. The strain-induced axial magnetic anisotropy obviously favors the DW oscillation and increases its amplitude, in agreement with earlier studies based on global permeability measurements.[57]

Micromagnetic calculations for a rectangular structure with $L$ = 5632 nm and $d$ = 20 nm confirm that for a fixed field value the DW displacement increases monotonously with induced UMA (Fig. 6d). Also, for this scenario an energy ansatz is able to explain the observed and simulated behavior, now with a modified stiffness parameter $c'$ (see ESI, Fig. S7 and ESI Note 7† for modified equations). The reduced stiffness (and thus restoring force) in case of an additional UMA enables the larger oscillation amplitudes.

an analytical dwell-time theory and including the convolution principle of MFM image formation we are able to model time-averaged MFM data and consequently determined DW oscillations for amplitudes down to 60 nm. In our current experimental ac-field setup, we are limited to frequencies of 1 kHz (due to an increase in coil's inductance and hence reduction in field amplitude at higher frequencies), but we do expect the method to work in a much larger frequency range, as long as the domain wall motion remains periodic and the detected phase signal averages during the integration time defined by tip speed and pixel size. The method however fails in the frequency range close to the resonance frequency $f_0$ of the cantilever, as there a more complex direct excitation of the cantilever will largely modify the measurement scheme. The developed dynamic imaging approach can be applied to any thin-film sample with well-defined zero-field DW equilibrium position and a displacement-dependent restoring force, in order to oscillate the DW periodically and repetitively. Although not tested experimentally in this work, deviations from a non-sinusoidal DW motion are expected to be detectable in the shape of the time-averaged MFM profile. To hint at this additional strength of the method, in Fig. S8 and Note 8 of the ESI,† the dwell time functions of periodic triangular and square-shaped DW movements are displayed. They clearly differ from that of a sinusoidal DW motion, and again bear a clear signature of the oscillation amplitude. A similar dwell-time function-based model is developed to analyze time-averaged dynamical difference images obtained by Kerr microscopy. As the image intensity is simply cumulated in time, also this method works independent of the DW frequency, provided the amplitudes are above optical resolution. With these techniques, the oscillation amplitude of the 180° DW in a permalloy Landau structure is found to be constant with frequency (up to studied 1 kHz) and to increase linearly with the excitation amplitude. The former signifies that DW mobility is large enough for the DW to instantaneously follow the applied field. For this frequency region, our findings are in good agreement with the reported data for Cobalt structures,[32] suggesting that the DW mobility of our $Ni_{81}Fe_{19}$ films is at least $10^5$ m s$^{-1}$ T$^{-1}$. Above findings are fully supported by micromagnetic simulations and can be understood by means of a simple domain model, which describes the excited Landau DW configuration as a forced damped harmonic oscillator, with the restoring force being influenced by size, thickness and anisotropy of the permalloy structure. Our new approach to time-averaged imaging and analysis of nanoscale DW oscillations is key to a more detailed understanding of DW dynamics.

## Conclusions

We developed a new approach for the direct imaging of periodic DW oscillations with nanoscale resolution using conventional MFM, and complemented these experiments on permalloy Landau structures with Kerr microscopy observations for oscillation amplitudes of micrometers and above. By means of

## Methods

### Planar rectangle fabrication

Planar permalloy ($Ni_{81}Fe_{19}$) rectangles of different sizes and thicknesses were prepared with a lift-off photoresist mask to define the geometry and *via* depositing permalloy by magnetron sputtering at room temperature.

## Rolling technology

Strain engineering based on a shapeable polymeric platform[58] was applied to prepare rolled-down[51] curved permalloy rectangles (rectangle 3′ in Fig. 6b and c). The stack of the three photosensitive polymer layers, namely the sacrificial layer (SL), stiff polyimide-based reinforcement layer (PI), and hydrogel-based swelling layer (HG) are spin-coated onto glass substrate. Using optical lithography, we design arrays of the polymer stacks in the form of rectangles with a typical size in the range of $3.5 \times 3.2$ mm$^2$. On top of the predetermined areas in the polymer layer stack, we prepare a lift-off photoresist mask to define the permalloy rectangle. The patterned polymeric platform is self-assembled into a 3D tubular structures by selectively etching the sacrificial layer in a water diluted solution of EDTA [Ethylenediaminetetraacetic acid, pH 7.0]. In the humid environment, the hydrogel-based polymer swells, generating mechanical stress in the plane parallel to the reinforcing polyimide layer. This leads to a downward bending of the polymer layer and initiates the rolling process. With a PI layer thickness of 1200 nm and a HG layer thickness of 500 nm, the final tube diameter in our experiments was 120 μm, with the permalloy structure placed on top of the tubes experiencing the same curvature as the tube.

## Kerr microscopy

A digitally enhanced wide-field Kerr microscope setup,[59] making use of the magneto-optical Kerr effect (MOKE) and equipped with an electromagnet, was applied for imaging the static and time-averaged dynamical domains of planar and rolled/curved permalloy rectangles. Throughout the paper, the longitudinal Kerr effect was applied at orthogonal planes of incidence with the magnetic field and magneto-optical sensitivity[60] being aligned along the rectangle's long axis. Coils are able to produce sinusoidal fields of a few mT up to kHz frequencies. Before observing the domain configuration, the ground state of the ferromagnetic rectangles was set by an ac-field demagnetizing procedure. Here an ac-field (frequency = 35 Hz, maximum amplitude = 20 mT, decay time to zero field = 5 s) was applied along the rectangle's long axis. The exposure time to capture a single frame was 0.05 s and the averaging of 128 frames therefore takes a total of 6.4 s to capture one image.

## Magnetic force microscopy

For MFM investigations, we used a Bruker Icon AFM and commercial high-resolution MFM tips with Co-alloy hard magnetic coating of thickness 20 nm, tip radius 15 nm, stiffness 2.8 N m$^{-1}$ and resonance frequency 75 kHz (Team Nanotec, MFM-ML1-225-C2.8). Measurements were performed in standard MFM lift mode with amplitude setpoint controlled tapping for the topography and phase shift measurement in an interleaved scan line with typical lift height of 30 nm. For capturing time dependent processes, the slow scan axis was disabled. To apply an in-plane external field to the sample, we use a home-build electromagnetic coil with ferrite core, which can be mounted on the MFM stage (Fig. S9 and Note 9 of the ESI†). It is capable of producing an in-plane field of magnitude $H_{max} = 0.25$ mT at a frequency = 1 kHz with a 10-volt ac-power supply.

## Micromagnetic simulations

Micromagnetic simulations were performed using the 3D object-oriented micromagnetic framework (OOMMF) code. The investigated volume was discretized by the finite difference method. We have chosen a cell size of $4 \times 4 \times 4$ nm$^3$ for rectangular elements up to a length of 5.6 μm and a cell size of $5 \times 5 \times 5$ nm$^3$ for rectangle of lengths ranging from 10 μm to 30 μm (Fig. 5) to speed up the simulation.

Simulation parameters for unstrained permalloy were taken as follows:[61] Saturation magnetization $M_s = 8 \times 10^5$ $A/m$, exchange constant $A = 1.3 \times 10^{-11}$ $J/m$, damping constant $\alpha = 0.02$. Simulations for quasi-static DW dynamics were performed in two following steps: (1) The initial magnetization was set to a two domain state, with magnetization parallel and antiparallel to the long axis of rectangle. Then the ground state (Landau structure) of the rectangles was achieved by a relaxation process in the absence of an external magnetic field. (2) The displaced equilibrium DW position was calculated by magnetization relaxation in the presence of a static magnetic field pointing along the rectangle's long axis. To extract the displaced DW position, we analyze the $m_y$ profile ($y$-component of normalized magnetization vector) across the 180° DW. The $x$-position of the DW is defined through the lowest absolute $m_y$ value. The field dependent DW displacement was evaluated by a successive increase of the field magnitude in steps of 0.1 mT in positive and negative $y$-direction with absolute maximum value of 1 mT. Selected micromagnetic simulations were performed with an additional uniaxial magnetic anisotropy ($K_u$) along the rectangle's long axis.

# Author contributions

D. K., V. N. and O. G. S. conceived the idea, V. N. designed the research, B. S. performed the experiments (sample preparation and characterization) and simulations and interpreted the data with help in sample preparation by R. R., in Kerr measurements by I. S. and R. S. and in micromagnetic simulations by J. A. O., V. N. supervised the experiments and data interpretation, B. S., V. N., D. K. and R. S. wrote the manuscript with the input from all other authors, and all authors contributed to the discussion of the results.

# Conflicts of interest

The authors declare no competing financial interest.

# Acknowledgements

# References

1 I. Betancourt, R. Valenzuela and M. Vazquez, Giant magnetoimpedance in Co-based microwires at low frequencies (100 Hz–13 MHz), *J. Appl. Phys.*, 2002, **91**, 8423.

2 R. Valenzuela and I. Betancourt, Giant magnetoimpedance, skin depth and domain wall dynamics. in IEEE International Digest of Technical Papers on Magnetics Conference vol. 38 CD1 (IEEE, 2002).

3 K. L. García and R. Valenzuela, Correlation between magnetization processes and giant magnetoimpedance response in CoFeBSi amorphous CoFeBSi wires, *J. Non-Cryst. Solids*, 2001, **287**, 313–317.

4 R. Valenzuela, Low-frequency magnetoimpedance: Domain wall magnetization processes, *Physica B: Condens. Matter*, 2001, **299**, 280–285.

5 R. Schäfer, I. Soldatov and S. Arai, Power frequency domain imaging on Goss-textured electrical steel, *J. Magn. Magn. Mater.*, 2019, **474**, 221–235.

6 B. Betz, *et al.*, Frequency-Induced Bulk Magnetic Domain-Wall Freezing Visualized by Neutron Dark-Field Imaging, *Phys. Rev. Appl.*, 2016, **6**, 1–7.

7 H. Richert, *et al.*, Dynamic Magneto-Optical Imaging of Domains in Grain-Oriented Electrical Steel, *Steel Res. Int.*, 2016, **87**, 232–240.

8 R. P. Harti, *et al.*, Dynamic volume magnetic domain wall imaging in grain oriented electrical steel at power frequencies with accumulative high-frame rate neutron dark-field imaging, *Sci. Rep.*, 2018, **8**, 1–7.

9 A. Sarella, A. Torti, M. Donolato, M. Pancaldi and P. Vavassori, Two-dimensional programmable manipulation of magnetic nanoparticles on-chip, *Adv. Mater.*, 2014, **26**, 2384–2390.

10 M. Donolato, *et al.*, On-Chip Manipulation of Protein-Coated Magnetic Beads via Domain-Wall Conduits, *Adv. Mater.*, 2010, **22**, 2706–2710.

11 M. Monticelli, *et al.*, On-Chip Magnetic Platform for Single-Particle Manipulation with Integrated Electrical Feedback, *Small*, 2016, **12**, 921–929.

12 E. Rapoport, D. Montana and G. S. D. Beach, Integrated capture, transport, and magneto-mechanical resonant sensing of superparamagnetic microbeads using magnetic domain walls, *Lab Chip*, 2012, **12**, 4433–4440.

13 B. Lim, P. Vavassori, R. Sooryakumar and C. Kim, Nano/micro-scale magnetophoretic devices for biomedical applications, *J. Phys. D: Appl. Phys.*, 2017, **50**, 033002.

14 G. S. D. Beach, M. Tsoi and J. L. Erskine, Current-induced domain wall motion, *J. Magn. Magn. Mater.*, 2008, **320**, 1272–1281.

15 G. Malinowski, O. Boulle and M. Kläui, Current-induced domain wall motion in nanoscale ferromagnetic elements, *J. Phys. D: Appl. Phys.*, 2011, **44**, 384005.

16 A. Yamaguchi, *et al.*, Real-Space Observation of Current-Driven Domain Wall Motion in Submicron Magnetic Wires, *Phys. Rev. Lett.*, 2004, **92**, 1–4.

17 G. S. D. Beach, C. Nistor, C. Knutson, M. Tsoi and J. L. Erskine, Dynamics of field-driven domain-wall propagation in ferromagnetic nanowires, *Nat. Mater.*, 2005, **4**, 741–744.

18 M. Hayashi, L. Thomas, C. Rettner, R. Moriya and S. S. P. Parkin, Direct observation of the coherent precession of magnetic domain walls propagating along permalloy nanowires, *Nat. Phys.*, 2007, **3**, 21–25.

19 G. Meier, *et al.*, Direct imaging of stochastic domain-wall motion driven by nanosecond current pulses, *Phys. Rev. Lett.*, 2007, **98**, 1–4.

20 E. Saitoh, H. Miyajima, T. Yamaoka and G. Tatara, Current-induced resonance and mass determination of a single magnetic domain wall, *Nature*, 2004, **432**, 203–206.

21 M. I. Khan, *et al.*, Current-induced domain wall oscillations in a nanowire imaged by time-resolved photoemission electron microscopy, *J. Magn. Magn. Mater.*, 2019, **476**, 538–545.

22 L. Bocklage, *et al.*, Time-resolved imaging of current-induced domain-wall oscillations, *Phys. Rev. B: Condens. Matter Mater. Phys.*, 2008, **78**, 3–6.

23 D. Bedau, *et al.*, Detection of current-induced resonance of geometrically confined domain walls, *Phys. Rev. Lett.*, 2007, **99**, 5–8.

24 D. Karnaushenko, *et al.*, Self–Assembled On–Chip–Integrated Giant Magneto–Impedance Sensorics, *Adv. Mater.*, 2015, **27**, 6582–6589.

25 B. Van Waeyenberge, *et al.*, Magnetic vortex core reversal by excitation with short bursts of an alternating field, *Nature*, 2006, **444**, 461–464.

26 M. I. Khan, *et al.*, Current-induced domain wall oscillations in a nanowire imaged by time-resolved photoemission electron microscopy, *J. Magn. Magn. Mater.*, 2019, **476**, 538–545.

27 M. Möller, J. H. Gaida, S. Schäfer and C. Ropers, Few-nm tracking of current-driven magnetic vortex orbits using ultrafast Lorentz microscopy, *Commun. Phys.*, 2020, **3**, 36.

28 A. Neudert, J. McCord, D. Chumakov, R. Schäfer and L. Schultz, Small-amplitude magnetization dynamics in permalloy elements investigated by time-resolved wide-

field Kerr microscopy, *Phys. Rev. B: Condens. Matter Mater. Phys.*, 2005, **71**, 134405.

29 D. Chumakov, *et al.*, Nanosecond time-scale switching of permalloy thin film elements studied by wide-field time-resolved Kerr microscopy, *Phys. Rev. B: Condens. Matter Mater. Phys.*, 2005, **71**, 014410.

30 N. O. Urs, *et al.*, Advanced magneto-optical microscopy: Imaging from picoseconds to centimeters - imaging spin waves and temperature distributions (invited), *AIP Adv.*, 2016, **6**, 055605.

31 C. V. Topping and S. J. A. C. Blundell, susceptibility as a probe of low-frequency magnetic dynamics, *J. Phys.: Condens. Matter*, 2019, **31**, 013001.

32 M. Kataja and S. van Dijken, Magneto-optical Kerr effect susceptometer for the analysis of magnetic domain wall dynamics, *Rev. Sci. Instrum.*, 2011, **82**, 103901.

33 K. Gross, K. Westerholt and H. Zabel, Domain wall dynamics of periodic magnetic domain patterns in Co 2 MnGe-Heusler microstripes, *New J. Phys.*, 2016, **18**, 033007.

34 K. L. Garciá and R. Valenzuela, Domain wall pinning, bulging, and displacement in circumferential domains in CoFeBSi amorphous wires, *J. Appl. Phys.*, 2000, **87**, 5257–5259.

35 I. Betancourt and R. Valenzuela, Magnetization Dynamics of Pinned Domain Walls in Partially Crystallized Ribbons, *IEEE Trans. Magn.*, 1997, **33**, 3973–3974.

36 S. T. Chui, Finite frequency dynamics of magnetic domain walls, *Phys. Rev. B: Condens. Matter Mater. Phys.*, 1999, **60**, 12219–12225.

37 O. Kazakova, *et al.*, Frontiers of magnetic force microscopy, *J. Appl. Phys.*, 2019, **125**, 060901.

38 R. Puttock, *et al.*, V-Shaped Domain Wall Probes for Calibrated Magnetic Force Microscopy, *IEEE Trans. Magn.*, 2017, **53**, 1.

39 S. Yoshimura, F. Zheng, S. Yasui, G. Egawa and H. Saito, AC Magnetic Field Imaging of Perpendicular Magnetic Write Head without Image Distortion on Alternating Magnetic Force Microscopy using a Cone-Shape FePt-coated Tip, *J. Magn. Soc. Jpn.*, 2018, **42**, 5–10.

40 M. Abe and Y. Tanaka, High frequency write head measurement with the phase detection magnetic force microscope, *J. Appl. Phys.*, 2001, **89**, 6766–6768.

41 M. R. Koblischka, J. D. Wei, M. Kirsch and U. Hartmann, High frequency magnetic force microscopy-imaging of harddisk write heads, *Jpn. J. Appl. Phys., Part 1*, 2006, **45**, 2238–2241.

42 Z. Li, *et al.*, AC driven magnetic domain quantification with 5â €...nm resolution, *Sci. Rep.*, 2014, **4**, 1–7.

43 R. Schäfer, Investigation of Domains and Dynamics of Domain Walls by the Magneto-optical Kerr-effect, in *Handbook of Magnetism and Advanced Magnetic Materials*, John Wiley & Sons, Ltd, 2007, DOI: **10.1002/ 9780470022184.hmm310**.

44 R. M. Bozorth, The permalloy problem, *Rev. Mod. Phys.*, 1953, **25**, 42–48.

45 D. Nečas, *et al.*, Determination of tip transfer function for quantitative MFM using frequency domain filtering and least squares method, *Sci. Rep.*, 2019, **9**, 3880.

46 A. Hubert and R. Schäfer, *Magnetic Domains: The Analysis of Magnetic Microstructures*, Springer, Berlin, 1998.

47 S. Konishi, T. Kusuda and S. Yamada, Domain-wall velocity, mobility, and mean-free-path in permalloy films, *IEEE Trans. Magn.*, 1971, **7**, 722–724.

48 K. Fukumoto, *et al.*, Mobility of domain wall motion in the permalloy layer of a spin-valve-like trilayer, *J. Magn. Magn. Mater.*, 2005, **293**, 863–871.

49 L. K. Bogart, D. S. Eastwood and D. Atkinson, The effect of geometrical confinement and chirality on domain wall pinning behavior in planar nanowires, *J. Appl. Phys.*, 2008, **104**, 033904.

50 B. Borie, A. Kehlberger, J. Wahrhusen, H. Grimm and M. Kläui, Geometrical dependence of domain-wall propagation and nucleation fields in magnetic-domain-wall sensors, *Phys. Rev. Appl.*, 2017, **8**, 1–8.

51 B. Singh, *et al.*, Self-assembly as a tool to study microscale curvature and strain-dependent magnetic properties, *npj Flexible Electron.*, 2022, **6**, 76.

52 H. Matsumoto, S. Ota, T. Koyama and D. Chiba, Control of magnetic anisotropy in a Co thin film on a flexible substrate by applying biaxial tensile strain, *Appl. Phys. Lett.*, 2021, **118**, 022406.

53 F. Zighem and D. Faurie, A review on nanostructured thin films on flexible substrates: links between strains and magnetic properties, *J. Phys.: Condens. Matter*, 2021, **33**, 233002.

54 R. Streubel, *et al.*, Magnetic microstructure of rolled-up single-layer ferromagnetic nanomembranes, *Adv. Mater.*, 2014, **26**, 316–323.

55 B. D. Cullity and C. D. Graham, *Introduction to Magnetic Materials*, John Wiley & Sons, Inc., 2008, DOI: **10.1002/ 9780470386323**.

56 R. Schäfer, *Handbook of Magnetism and Magnetic Materials*, Springer International Publishing, Cham, 2021, DOI: **10.1007/978-3-030-63101-7**.

57 M. T. González, K. L. García and R. Valenzuela, Circumferential magnetization curves of Co-rich amorphous wires under tensile stress, *J. Appl. Phys.*, 1999, **85**, 319–324.

58 D. D. Karnaushenko, D. Karnaushenko, D. Makarov and O. G. Schmidt, Compact helical antenna for smart implant applications, *NPG Asia Mater.*, 2015, **7**, 1–10.

59 I. V. Soldatov and R. Schäfer, Selective sensitivity in Kerr microscopy, *Rev. Sci. Instrum.*, 2017, **88**, 073701.

60 I. V. Soldatov, *et al.*, Advanced, Kerr-microscopy-based MOKE magnetometry for the anisotropy characterisation of magnetic films, *J. Magn. Magn. Mater.*, 2021, **529**, 167889.

61 W. J. Kim, T. D. Lee, S. H. Choa, S. M. Seo and K. J. Lee, Effect of ac on current-induced domain wall motion, *J. Appl. Phys.*, 2007, **101**, 7–10.